Research Article Vol. 4, No. 8 / 15 Aug 2021 / OSA Continuum 2364

Beam shape modification due to the non-linear optical response in a dense rubidium vapor

A. J. VAN LANGE, S. P. VAN SOLINGE, G. BUIST, AND D. VAN OOSTEN*

Debye Institute for Nanomaterials Science and Center for Extreme Matter and Emergent Phenomena, Utrecht University, Princetonplein 5, 3584 CC Utrecht, The Netherlands
D.vanOosten@uu.nl

Abstract: Dense atomic vapors have strong non-linear optical properties for near-resonant light. As a result, an initially Gaussian beam profile is strongly distorted due to propagation through such a dense vapor, leading to various distinct beam profiles. In our experiment, we track the detuning from resonance at which these beam profiles occur as a function of intensity. We establish a detuning curve as a function of intensity for each shape at two different cell temperatures. After proper scaling, the detuning curves all collapse onto one universal detuning curve, which suggests that the shapes are manifestations of the same underlying phenomenon.

1. Introduction

Since the invention of the laser it was clear that the high intensities offered by this light source could give rise to nonlinear optical effects. Beam profiles of laser beams are heavily affected by these non-linearities. Pioneers like Bloembergen and Townes already saw evidence of self-focusing [1,2] and more recently, the propagation of light in nonlinear optical media has been seen to give rise to optical solitons, that maintain their spatial profile and/or (in the case of pulsed lasers) their temporal shape [3–9]. From a theoretical point of view, the physics of the propagation of laser beams through nonlinear optical media strongly resembles the physics of interacting Bose-Einstein condensates; both can be accurately described using the nonlinear Schrödinger equation [10–12]. This similarity has been exploited to demonstrate superfluid-like behaviour in optical propagation [13–17]. Dense alkali vapors are an extremely versatile platform to carry out such experiment, because strength and sign of the nonlinearity can be chosen by adjusting the detuning (with respect to the resonance frequency). They have recently regained interest for their ability to affect the statistics and beam shape of near-resonant laser light. Below the transition frequency, *i.e.* at negative detuning with respect to the atomic resonance, defocusing causes intriguing effects in beam statistics: a disorganised speckle pattern regains coherence gradually due to the defocusing nonlinearity [18] and the beam profile evolution in the cell is found to be analogous to the time-evolution of a 2D-Bose gas [19–21].

Above the transition frequency, *i.e.* at positive detuning with respect to the atomic resonance, beams with extraordinary shapes have been observed emerging from a dense alkali vapor. Already in the 70s and 80s, alkali vapors were shown to have a self-focusing effect on blue-detuned laser beams [3,22]. More recently, Gaussian beams of nearly resonant light, were found to exhibit exotic beam profiles after propagation through a hot dense rubidium vapor [23]. Near-resonant laser beams focused strongly in the non-linear medium have been used to produce Bessel-Gauss modes, which have self-reconstructing properties upon hitting an obstacle [24]. Under slightly different conditions cross-phase modulation produces size-variable Dark-Hollow Beams (DHB): optical modes with a bright ring around a dark centre [25], which can be turned into a self-healing Bessel beam by focusing.

In this work, we report on transmission experiments performed with high laser intensity and at high atomic densities. Various characteristic shapes are observed emerging from the dense

#432780 https://doi.org/10.1364/OSAC.432780
Journal © 2021 Received 31 May 2021; revised 12 Jul 2021; accepted 12 Jul 2021; published 8 Aug 2021

OSA CONTINUUM

rubidium vapor cell, examples of which are shown in Fig. 1. These shapes appear at a different detuning for each beam intensity and temperature, are very robust, easily reproducible and highly similar for different detuning-intensity-temperature combinations. We track the detuning at which the characteristic shapes appear over a range of intensities and find that the detuning curves of the characteristic shapes collapse onto one universal dimensionless detuning curve.

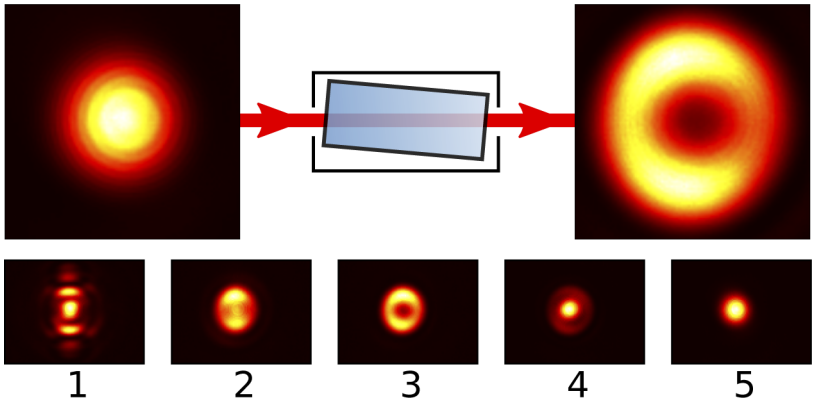

Fig. 1. The basic concept of the experiment: the incoming laser beam profile changes shape after propagation through a dense rubidium vapor. The bottom row shows typical shapes emerging from the dense rubidium vapor.

2. Setup

Initial experiments were carried out using the setup described in [26]. For follow-up experiments, an adapted version shown in Fig. 2 was used. The most important difference between the setups is that in [26] an extended cavity diode laser was used, with analog control of the optical frequency and a mode-hop free range of only a few GHz, whereas the setup presented here uses a distributed feedback (DFB) laser diode. The DFB laser is computer controlled and has a large mode-hop free range, allowing us to readily perform optical frequency scans of several tens of GHz. Light from the DFB diode is amplified in a fiber coupler semiconductor optical amplifier (SOA) and a tapered amplifier. The resulting light is spatially filtered to produce an approximately Gaussian beam with a waist $w_0 = 850$ μm and attenuated to the desired power. The optical frequency is measured using a wavemeter (HighFinesse WS6-600), with an absolute accuracy of 600 MHz and a wavelength deviation sensitivity of 20 MHz. The Gaussian beam is sent through a 10 cm long heated rubidium cell with a natural isotope ratio. The resulting profile of the beam that exits the cell is recorded using two cameras. One records a near-field image of the beam at the exit window of the heated cell containing a dense rubidium vapor, the other records a far-field beam profile. The near-field image is measured in a 4f configuration in the following way. Output light is deflected by a 92%:8% pellicle beam splitter and collected by a 2" lens positioned at a focal length distance, $d = f = 100$ mm. A second $f = 100$ mm lens forms the image on the camera. At high beam powers, attenuators are placed in front of the cameras.

OSA CONTINUUM

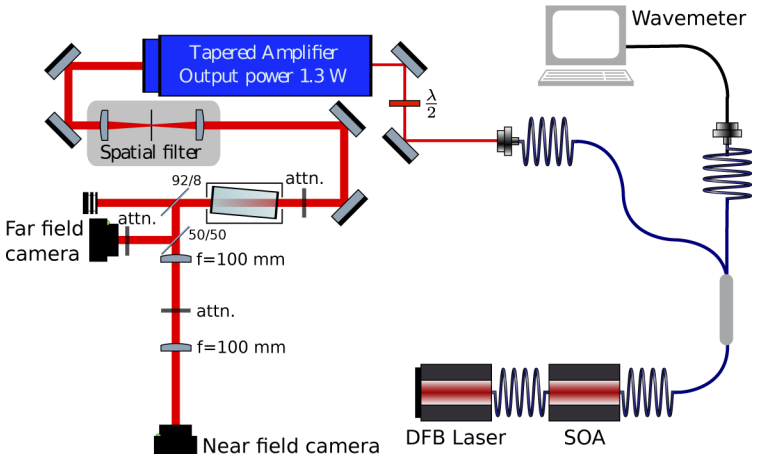

Fig. 2. The setup to record the beam profile of output beam after propagation through a dense rubidium vapor. From the diode laser light source, the light is first amplified by a fiber coupled semiconductor optical amplifier (SOA). Part of the amplified light is fiber coupled to a wavemeter (HighFinesse WS-6 wavemeter). The majority of the light is used to seed a tapered amplifier (Toptica BoosTA). The light is subsequently spatially filtered and attenuated to the desired power. The rubidium cell is in an oven, consisting of a heat shield with isolation and heating wires. The temperature of the cell (denoted T_{tc}) is measured with a thermocouple. The profile of the outgoing beam is measured using a Point Grey Chameleon camera. Additionally, the exit window of the cell is also imaged by a 4-f imaging system.

3. Results

To get an initial sense of the kind of shapes emerging from the cell at different conditions, the beam profiles (as measured on the far-field camera using the setup of Fig. 2) are displayed on a grid of intensity and detuning in Fig. 3. The detuning is defined with respect to the line strength weighted average of the transition frequencies of the ^{87}Rb $F = 1 \rightarrow F' = 0, 1, 2$ transitions. The beam profiles are measured at equidistant steps in detuning and for different incident powers. For clarity, we only present a subset of the data; the full set contains images for 15 incident beam powers and 361 detunings, all of which are available in Dataset 1 [27]. In the resulting array of pictures, two remarkable features catch the eye: self-focusing and ring formation.

Far above the resonance and for lower incident power (*i.e.* the bottom right image in the figure), the beam profile is roughly Gaussian. When the resonance is approached from above (going from right to left in the figure) or when the incident power is increased (going from the bottom to the top in the figure), the width of the profile first becomes smaller and smaller, but the profile still resembles a Gaussian. This effect is clearly visible in the bottom two rows, where the beam diameter shrinks to roughly half the original size. The shrinking of the beam diameter is attributed to the self-focusing of the beam in the dense rubidium vapor. [3,22]

The second eye-catching feature is the appearance of a ring shaped profile for sufficiently high power and low detuning. Interestingly, these positions seem to follow a curve with a specific relation between detuning and intensity, as we have illustrated by highlighting a particular beam shape in the figure.

Lastly, we note that for the smallest detunings (the left-most column in Fig. 3 and profile 1 in Fig. 1) the profiles are clearly not rotationally symmetric. We verified that the appearance of these non-rotationally symmetric shapes does not depend on the incident polarization. We

OSA CONTINUUM

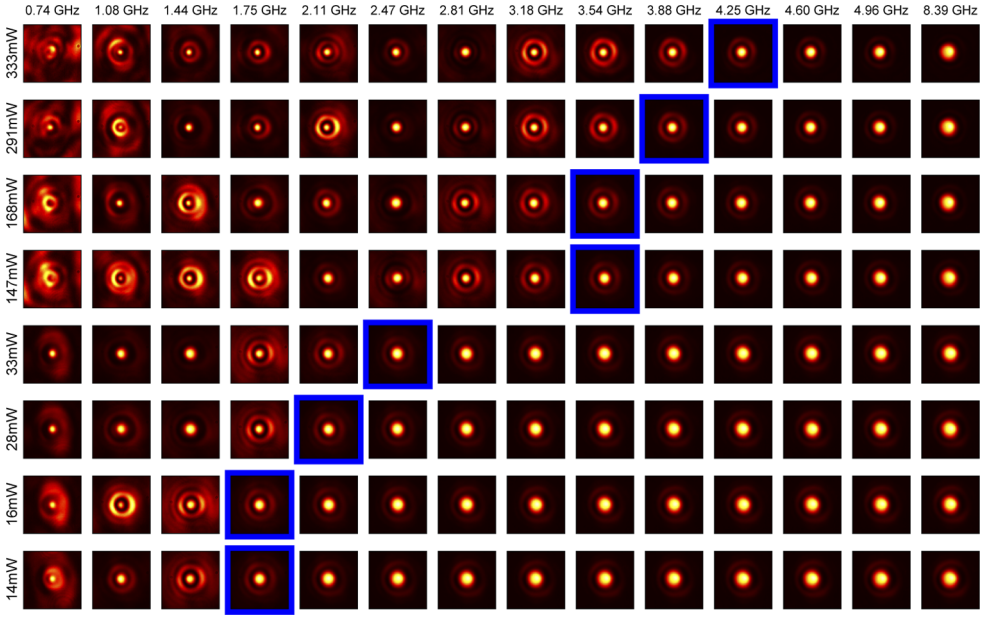

Fig. 3. Emerging beam profiles as a function of incident power and detuning with respect to the (line strength weighted) average transition frequency of the ^{87}Rb $F = 1 \rightarrow F' = 0, 1, 2$ transitions (384.23458 THz). The cell temperature during these measurements was $T_{tc} = 166°C$. The power range corresponds to a peak s_0 of the Gaussian beam of $1.3 \cdot 10^3$ to $2.6 \cdot 10^4$.

therefore attribute it to the fact that the incident beam is not perfectly Gaussian and not completely rotationally symmetric, which we verified by performing experiments with a beam rotator.

To uncover the relation we track the detuning of this shape (and others) over the whole power range. Specifically, we track the detuning at which the characteristic shapes of Fig. 1 occur as a function of saturation parameter $s_0 = I/I_s$, with I_s the saturation intensity. For each s_0, we manually vary the detuning to find the profile that is most similar to the characteristic shape. Similarity to the reference image is quantified using the structural similarity index (SSIM) of two images [28]. By definition, the SSIM index ranges from −1 to 1, where 1 indicates perfect similarity between identical images, 0 indicates all structural similarity between the images is lost and negative values indicate the image structure is inverted. We have chosen to optimise the SSIM value rather than to minimise the mean squared error, because SSIM deals better with noise, local disturbances and offsets [29,30]. Because we want to track shapes that are qualitatively similar, the images are allowed to undergo affine transformations, such as displacement, scaling, shearing and rotation, while determining the optimum SSIM value. In practice, only the scaling turns out to be relevant. This procedure is further explained and illustrated in Sec. S1 of Supplement 1. We carry out this experiment at two different cell temperatures ($T_{tc} = 166°C$ and $184°C$) corresponding to different vapor densities ($\rho = 0.8 \times 10^{19}$ m^{-3} and 2.6×10^{19} m^{-3}, respectively, as established in [26]).

The characteristic shapes from Fig. 1, numbered from 1 to 5, are used as reference signal for the shape tracking. The optimum in SSIM between the reference image and the image at a different input power P_{in} is determined while varying the laser frequency, which results in a detuning curve $\delta_i(s_0)$ for each shape i. The resulting detuning curves $\delta_i(s_0)$ are shown in Fig. 4, where the bare peak s_0 is determined by I_{peak}/I_s, where $I_{peak} = 2P_{in}/(\pi w_0^2)$. The SSIM values we find for optimum similarity range from 1 at the reference image to a minimum of 0.7, which still

OSA CONTINUUM

indicates a high level of similarity. Importantly, as illustrated in Fig. S1 of Supplement 1, the SSIM value has a clear maximum in detuning at each s_0, making the method well suited for the tracking of specific shapes. In all the experiments, the optimal scaling is typically a few percent, as shown in Figs. S2 and S4 of Supplement 1.

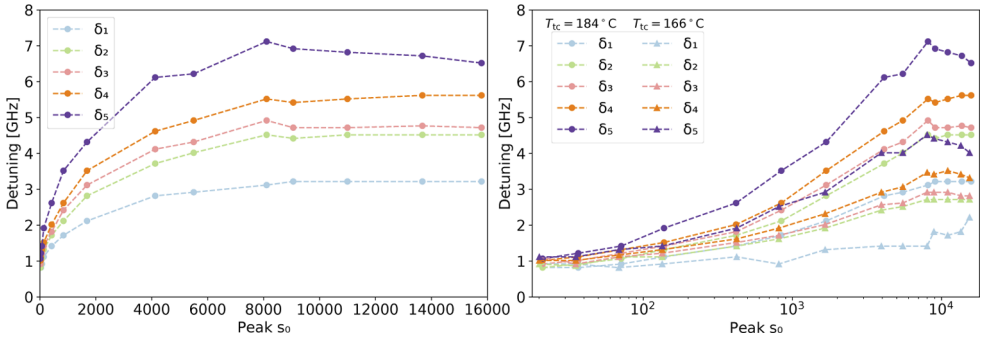

Fig. 4. Tracking of characteristic beam profiles. (a) Detuning curve δ_i for the five characteristic beam profiles as function of s_0 on a linear scale for $T_{tc} = 184°C$ and (b) on a logarithmic scale for $T_{tc} = 166°C$ and $T_{tc} = 184°C$.

All detuning curves δ_i in Fig. 4(a) depend on s_0 in a similar fashion: starting from a small, non-zero value, a very sharp initial increase is steadily converted to a gentle increase until it levels out at $s_0 \gtrsim 8 \cdot 10^3$ to a final value $\delta_{i,\mathrm{fin}}$ between 3 and 7 GHz. In Fig. 4(b), we show data for two different cell temperatures, but now on a logarithmic scale. The curves show similar behaviour for both temperatures, but with a different amplitude. We also see that all curves tend to the same small value of ~ 800 MHz for small saturation parameters. An exception to this is curve δ_1 for $T_{tc} = 166°C$, which looks significantly noisier than the other curves. We attribute this to the fact that for the lower cell temperature, this beam shape could only be found for very small detunings, which led to a difficult and therefore perhaps inaccurate measurement. We included the data nonetheless, for completeness.

4. Universal detuning curve

The similarity between all the detuning curves $\delta_i(s_0)$ suggests there is a universal relation between δ and s_0, of which the individual δ_i's are special cases. To unveil this universal behaviour, the curves are collapsed onto the same line by the following procedure. An offset of δ_{offset} is applied to all δ_i's, which are subsequently divided by their final value for high s_0 (corrected for δ_{offset}), yielding a normalised dimensionless detuning of

$$\bar{\delta}_i(s_0) = \frac{\delta_i(s_0) - \delta_{\mathrm{offset}}}{\delta_{i,\mathrm{fin}} - \delta_{\mathrm{offset}}}, \tag{1}$$

where $\delta_{i,\mathrm{fin}}$ is determined by the average of the last three data points in the curves for $\delta_i(s_0)$.

For all δ_i's this gives similar $\bar{\delta}_i$ curves, for which we can make the collapse complete by determining the correct offset. Only the curve $\delta_1(166°C)$ is itself too erratic to produce a reasonable $\bar{\delta}_1$ curve. It is therefore discarded in the analysis to determine the universal detuning curve. The optimum of offset $\delta_{\mathrm{offset}} = 778$ MHz is determined by minimising the sum of standard deviations of $\bar{\delta}_i$'s per s_0. This is further explained in Sec. S2 of Supplement 1.

Figure 5 shows this collapse procedure to be very effective for all $\bar{\delta}_i$, except for $\bar{\delta}_1$ (166°C). With this universal detuning curve, a full detuning curve of any characteristic beam shape can be recovered from just its final detuning $\delta_{i,\mathrm{fin}}$, using the inverse of Eq. (1). For $s_0 \lesssim 8 \cdot 10^3$, the universal detuning curve can be captured in a fit function $\bar{\delta}(s_0) = a + b \cdot {s_0}^c$, with $a = -0.1 \pm 0.03$,

OSA CONTINUUM

$b = 0.05 \pm 0.01$ and $c = 0.35 \pm 0.02$. The universal curve for the dimensionless detuning thus

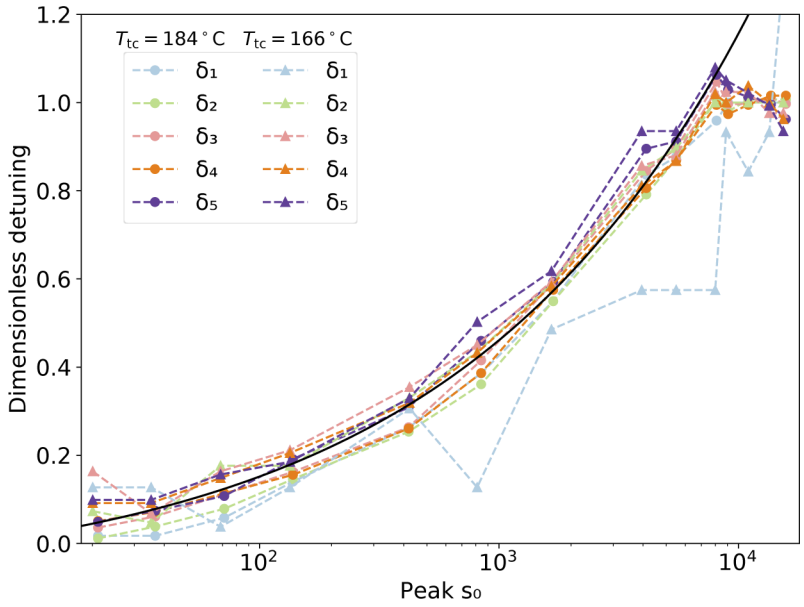

Fig. 5. The collapse of the detuning curves on the universal dimensionless detuning curve $\bar{\delta}$, which is given by Eq. (1). The black dashed line is the fit for $\bar{\delta} = a + b\ {s_0}^c$, with $a = -0.1 \pm 0.03$, $b = 0.05 \pm 0.01$ and $c = 0.35 \pm 0.02$.

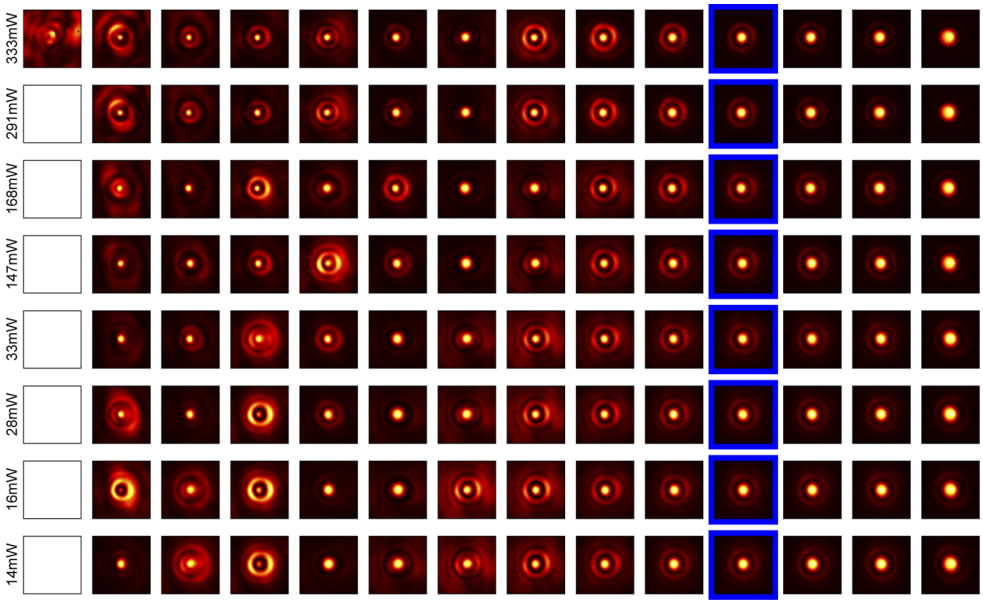

Fig. 6. Emerging beam profiles for various incident powers and detunings. The top row is the same as that of Fig. 3, but the remaining images in each column are selected based on Eq. 1, which predicts the detuning at which similar looking profiles should emerge for a given incident saturation intensity.

OSA CONTINUUM

appears to be proportional to $\sqrt[3]{s_0}$ for $s_0 < 10^4$. This is curious, as one perhaps would rather expect a relationship to power broadening, which goes as $\sqrt{1+s_0}$.

Figure 6 allows us to visually verify that similar beam shapes are indeed produced at detunings predicted by the above fit of $\bar{\delta}(s_0)$. In this figure, the images in the top row are images obtained at a given power and a given detuning, identical to the top row of Fig. 3. In each subsequent row (corresponding to a lower incident laser power), images corresponding to a detuning predicted by the universal detuning curve are shown. Please note that for the left-most column, the universal detuning curve cannot be used as it corresponds to a detuning smaller than δ_{offset}. As demonstrated by the highlighting, the images in each column now indeed show a great similarity, for detunings $\gtrsim 3.5$ GHz. For detunings $\lesssim 3.5$ GHz, the similarity within the columns is clearly reduced, indicating that the universal detuning curve is more accurate for larger detunings. The fact that the universal detuning curve is most accurate for larger detunings, gives hope that a theoretical description in terms of a single Lorentzian line could suffice [18] as opposed to a more elaborate model [26].

5. Conclusion

In our experiments we observe stable, robust optical profiles, spontaneously formed from an almost Gaussian input profile by non-linear effects in dense rubidium vapors at a high saturation parameter. The specific shape of the profiles and especially the fact that some profiles break rotational symmetry, might have its origins in the fact that the incident beam profile deviates from a perfect Gaussian beam. Curiously, the profiles occur at very specific combinations of the saturation parameter and detuning, which we captured in detuning curves $\delta_i(s_0)$ for each shape i for a given temperature. All the detuning curves collapse onto a universal dimensionless detuning curve, which indicates that the shapes are manifestations of the same phenomenon. We currently lack a theoretical explanation for this universal behaviour, which holds for more than two orders of magnitude in saturation parameter. The tantalising simplicity of the universal detuning curve, suggests that there should be an elegant theoretical explanation for its form.

Funding. Nederlandse Organisatie voor Wetenschappelijk Onderzoek.

Acknowledgments. The authors thank Paul Jurrius, Dante Killian, Aron Opheij and Cees de Kok for technical support.

Disclosures. The authors declare that there are no conflicts of interest related to this article.

Data availability. Data underlying the results presented in this paper are available in Ref. [27].

Supplemental document. See Supplement 1 for supporting content.

References

1. P. Lallemand and N. Bloembergen, "Self-focusing of laser beams and stimulated raman gain in liquids," Phys. Rev. Lett. **15**(26), 1010–1012 (1965).
2. E. Garmire, R. Y. Chiao, and C. H. Townes, "Dynamics and characteristics of the self-trapping of intense light beams," Phys. Rev. Lett. **16**(9), 347–349 (1966).
3. J. E. Bjorkholm and A. A. Ashkin, "cw self-focusing and self-trapping of light in sodium vapor," Phys. Rev. Lett. **32**(4), 129–132 (1974).
4. L. F. Mollenauer, R. H. Stolen, and J. P. Gordon, "Experimental observation of picosecond pulse narrowing and solitons in optical fibers," Phys. Rev. Lett. **45**(13), 1095–1098 (1980).
5. A. Barthelemy, S. Maneuf, and C. Froehly, "Propagation soliton et auto-confinement de faisceaux laser par non linearité optique de kerr," Opt. Commun. **55**(3), 201–206 (1985).
6. Y. Silberberg, "Collapse of optical pulses," Opt. Lett. **15**(22), 1282–1284 (1990).
7. J. S. Aitchison, A. M. Weiner, Y. Silberberg, M. K. Oliver, J. L. Jackel, D. E. Leaird, E. M. Vogel, and P. W. E. Smith, "Observation of spatial optical solitons in a nonlinear glass waveguide," Opt. Lett. **15**(9), 471–473 (1990).
8. M. Segev, B. Crosignani, A. Yariv, and B. Fischer, "Spatial solitons in photorefractive media," Phys. Rev. Lett. **68**(7), 923–926 (1992).
9. O. Lahav, O. Kfir, P. Sidorenko, M. Mutzafi, A. Fleischer, and O. Cohen, "Three-dimensional spatiotemporal pulse-train solitons," Phys. Rev. X **7**(4), 041051 (2017).
10. E. P. Gross, "Structure of a quantized vortex in boson systems," Nuovo Cim **20**(3), 454–477 (1961).

OSA CONTINUUM

11. L. P. Pitaekvskii, "Vortex lines in an imperfect bose gas," Phys. Rev. **151**(1), 100–104 (1966).
12. V. I. Karpman and E. M. Krushkal, "Modulated waves in nonlinear dispersive media," J. Phys. Soc. Jpn. **32**(1), 260–269 (1972).
13. C. Sun, S. Jia, C. Barsi, S. Rica, A. Picozzi, and J. W. Fleischer, "Observation of the kinetic condensation of classical waves," Nat. Phys. **8**(6), 470–474 (2012).
14. W. Wan, S. Jia, and J. W. Fleischer, "Dispersive superfluid-like shock waves in nonlinear optics," Nat. Phys. **3**(1), 46–51 (2007).
15. C. Michel, O. Boughdad, M. Albert, P.-É. Larré, and M. Bellec, "Superfluid motion and drag-force cancellation in a fluid of light," Nat. Commun. **9**(1), 2108 (2018).
16. D. Vocke, C. Maitland, A. Prain, K. E. Wilson, F. Biancalana, E. M. Wright, F. Marino, and D. Faccio, "Rotating black hole geometries in a two-dimensional photon superfluid," Optica **5**(9), 1099–1103 (2018).
17. A. Prain, C. Maitland, D. Faccio, and F. Marino, "Superradiant scattering in fluids of light," Phys. Rev. D **100**(2), 024037 (2019).
18. N. Šantic, A. Fusaro, S. Salem, J. Garnier, A. Picozzi, and R. Kaiser, "Nonequilibrium Precondensation of Classical Waves in Two Dimensions Propagating through Atomic Vapors," Phys. Rev. Lett. **120**(5), 055301 (2018).
19. A. Aprá, Superfluidity of light in a nonlinear atomic medium Ph.D. thesis, Sapienza Universitá di Roma (2017)..
20. Q. Fontaine, T. Bienaimé, S. Pigeon, E. Giacobino, A. Bramati, and Q. Glorieux, "Observation of the Bogoliubov Dispersion in a Fluid of Light," Phys. Rev. Lett. **121**(18), 183604 (2018).
21. Q. Fontaine, P.-E. Larré, G. Lerario, T. Bienaimé, S. Pigeon, D. Faccio, I. Carusotto, E. Giacobino, A. Bramati, and Q. Glorieux, "Interferences between bogoliubov excitations in superfluids of light," Phys. Rev. Research **2**(4), 043297 (2020).
22. M. G. Boshier and W. J. Sandle, "Self-focussing in a vapour of two-state atoms," Opt. Commun. **42**(5), 371–376 (1982).
23. Y. Zhang, X. Cheng, X. Yin, J. Bai, P. Zhao, and Z. Ren, "Research of far-field diffraction intensity pattern in hot atomic Rb sample," Opt. Express **23**(5), 5468 (2015).
24. J. D. Swaim, K. N. David, E. M. Knutson, C. Rios, O. Danaci, and R. T. Glasser, "Atomic vapor as a source of tunable, non-Gaussian self-reconstructing optical modes," Sci. Rep. **7**(1), 42311 (2017).
25. Q. Zhang, X. Cheng, B. He, H. Chen, Z. Ren, and J. Bai, "Size-variable dark-hollow beam generation using cross-phase modulation," Optics and Laser Technology **119**, 105582 (2019).
26. A. J. van Lange, P. van der Straten, and D. van Oosten, "Combined effect of non-linear optical and collisional processes on absorption saturation in a dense rubidium vapour," J. Phys. B: At., Mol. Opt. Phys. **53**(12), 125402 (2020).
27. S. P. van Solinge, A. J. van Lange, and D. van Oosten, "Beam shape modification due to the non-linear optical response in a dense rubidium vapor: code and data,", Utrecht University (2021). https://doi.org/10.24416/UU01-PS06RY.
28. Z. Wang, A. Bovik, H. Sheikh, and E. Simoncelli, "Image Quality Assessment: From Error Visibility to Structural Similarity," IEEE Trans. on Image Process. **13**(4), 600–612 (2004).
29. Z. Wang, A. C. Bovik, and E. P. Simoncelli, "Structural Approaches to Image Quality Assessment," in *Handbook of Image and Video Processing*, (Elsevier, 2005), pp. 961–974.
30. Z. Wang and A. C. Bovik, "Mean squared error: Love it or leave it? A new look at Signal Fidelity Measures," IEEE Signal Process. Mag. **26**(1), 98–117 (2009).